3D Printing of Customizable Transient Bioelectronics and Sensors

Nicolas Fumeaux and Danick Briand*

Transient electronics have emerged as a new category of devices that can degrade after their functional lifetime, offering tremendous potential as disposable sensors, actuators, wearables, and implants. Additive manufacturing methods represent a promising approach for patterning transient materials, yet examples of fully printed bioelectronic devices are scarce. This study introduces a fully digital 3D printing approach enabling the prototyping and customization of soft bioelectronics made of transient materials. The direct ink writing of poly(octamethylene maleate (anhydride) citrate) (POMaC) as an elastomeric matrix and of a shellac-carbon ink as a conductor is investigated. Precise and repeatable deposition of both structural and conductive features is achieved by optimizing printing parameters, i.e., the dispense gap, printing speed, and inlet pressure. Multi-material 3D printing enables the fabrication of functional transient devices. Notably, pressure and strain sensors are shown to operate in ranges relevant to implanted biomechanical monitoring. 3D-printed transient electrodes are demonstrated to be comparable to state-of-the-art devices in terms of impedance behavior. Finally, physical degradation of the materials is confirmed at physiological conditions. These fully digital additive manufacturing processes enable the monolithic fabrication of customizable transient bioelectronics with adaptable functions and geometries.

1. Introduction

In the past decade, transient electronics have garnered significant interest as temporary bioelectronic devices capable of fulfilling monitoring, stimulation, or actuation functions for a limited period of time.[1–3] These devices are designed to degrade in the environment or within the body without causing adverse side effects.[4] In the case of biodegradable or ecoresorbable devices, their degradability allows to reduce electronic waste.[3] When it comes to bioresorbable implants, degradation can allow notably to avoid re-operation in cases where only short-term functionality is needed and may help reduce inflammatory response by providing a dissolvable interface with the tissue.[5] This emerging class of devices relies on materials that undergo degradation in biological environments through hydrolysis or enzymatic processes, posing a significant challenge to their fabrication due to this inherent property. Several approaches have been proposed to tackle this challenge, such as mask-based deposition,[6] or transfer methods relying on controlled adhesion with a silicone stamp.[7] or lamination of films using bioresorbable adhesives.[8] These strategies have resulted in a diverse range of transient wearable or implantable devices, including pressure,[9] temperature,[10] and strain[11] sensors, electrocorticography (ECoG) electrodes[12] and pacemaker leads.[13]

Additive manufacturing (AM) has emerged as a promising approach for fabricating transient electronics from degradable materials.[14,15] Compared to the methods used thus far, additive manufacturing presents the advantage of enhanced compatibility with transient materials. Indeed, transient materials are typically more sensitive to increased temperatures or the use of solvents during the fabrication process. Additive manufacturing also opens the possibility for the monolithic fabrication of functional devices, eliminating the need for complex or manual assembly techniques. Furthermore, by using 3D printing techniques, AM has proven highly compatible with soft materials, facilitating the fabrication of complex structures using elastomers or hydrogels.[16] The successful integration and operation of bioelectronic wearables or implants critically relies on conformability and matching mechanical properties with the local tissue.[17–19] In this context, advancements in the field have prominently focused on the utilization of soft and elastic materials, driving significant progress.[20] Lastly, 3D digital additive manufacturing is being considered for the customization of wearables[19,21] and electronic implants,[22] providing a high degree of adaptation to the anatomy and complex geometries of the human body. The digital aspect of 3D additive manufacturing techniques allows for the seamless translation from a design to a device without adaptations to the process or designing and fabricating masks. This facilitates the rapid prototyping

N. Fumeaux, D. Briand
Soft Transducers Laboratory
Ecole Polytechnique Fédérale de Lausanne (EPFL)
Rue de la Maladière 71b, Neuchâtel CH-2000, Switzerland
E-mail: danick.briand@epfl.ch

The ORCID identification number(s) for the author(s) of this article can be found under https://doi.org/10.1002/aelm.202400058

**ADVANCED
SCIENCE NEWS**

www.advancedsciencenews.com

**ADVANCED
ELECTRONIC
MATERIALS**

www.advelectronicmat.de

of bioelectronics, and allows for the modification of geometries and functions specific to a targeted organ or application. This opportunity has been recognized in the field of neuromuscular interfaces, with the emergence of customizable, additively manufactured bioelectronic implants.[22–25] Direct-ink writing (DIW), in particular, holds promise for that purpose, thanks to the versatility in terms of inks and materials that can be printed,[26] enabling the multi-material manufacturing of complex devices using a single printer. Indeed, while other digital methods such as inkjet printing or digital light processing allows for rapid customization, they are limited whether in terms of ink viscosity or the use of conductive fillers.[27,28]

Various materials including transient elastomers and hydrogels have been printed, principally for tissue engineering applications. Efforts on 3D printing bioresorbable elastomers have centered around poly(glycerol sebacate) (PGS). PGS can be rendered polymerizable by UV light with the addition of acrylate,[29] methacrylate,[30] or cinnamate reactive groups.[31] PGS has been 3D printed using methods such as digital light processing,[32] 2-photon polymerization,[30] or direct ink writing.[33,34] Poly(octamethylene maleate (anhydride) citrate) (POMaC) is a more recently introduced bioresorbable polymer, which is readily UV-curable. Investigations in the printability of POMaC are limited to a recent publication, where POMaC is printed by DIW in the form of a copolymer with poly(ethylene glycol) diacrylate (PEGDA).[35] Degradable hydrogels (such as PEGDA, alginate, or gelatin-based gels) have also been 3D printed to form microfluidic channels[36] or scaffolds to promote regeneration in vivo,[37,38] principally using direct ink writing. Integrating electronics on hydrogels is notably difficult due to their mechanical mismatch with typical conductors.[25] Some printable transient hydrogels presented in the literature boast interesting properties, such as shape-memory behavior[39,40] for actuators, or ionic[40,41] or electrical[37,42] conductivity. However, the conductivities obtained for transient hydrogels are typically low (<1 S m^{-1}).

Printable transient materials with higher conductivities have been developed. Metallic pastes based on zinc have been proposed with conductivities exceeding 10^6 S m^{-1}.[43–45] These have however not been 3D printed yet, likely because they require local sintering approaches to reach an acceptable conductivity. A demonstration of zinc direct ink writing has been recently published,[46] however, the structures require annealing at 600 °C, which is incompatible with transient polymers. Electrically conductive transient pastes that could be compatible with 3D printing and require no complex or high-temperature curing have been proposed. Carbon- and graphite-based transient inks have been 3D printed by direct ink writing.[47,48] Similarly, various ink formulations utilizing molybdenum[49] or tungsten[50] have been developed, exhibiting conductivities in the range of several kS m^{-1}. Despite these advancements, the digital 3D additive manufacturing of transient bioelectronics remains a challenge, and necessitates the seamless integration of structural and conductive inks in a cohesive fabrication process.

In this work, we pioneer the fully digital additive manufacturing of transient bioelectronics and sensors by direct ink writing. The DIW of POMaC elastomer is thoroughly studied to achieve precise and repeatable deposition of features with lines in the order of 200–300 µm in width and a thickness of ≈50 µm. A slow-degrading, water-resistant shellac-carbon ink is used as a func-

tional material for the formation of conductive traces embedded in a POMaC matrix. The inks are deposited in a multi-nozzle 3D printer, enabling the monolithic fabrication of functional transient electronics within a single machine. The physical degradation behavior of the materials used in this work is studied at physiological conditions and under accelerated hydrolysis. The additive process is exploited to fabricate transient pressure and strain sensors as well as recording electrodes, whose sensing characteristics are evaluated for applications as degradable bioelectronics.

2. Results and Discussion

2.1. Approach and Materials

As introduced above, we studied the fabrication of transient bioelectronics by 3D printing, with the aim of enabling the customization of these devices in terms of geometry, design, and function. This concept is illustrated in **Figure 1a**, which shows the pipeline for customization of transient electronics and their subsequent facile fabrication using direct ink writing. By employing multi-nozzle printing and UV curing within the same machine, the digital design file can be directly translated into a personalized transient electronic device with a specific function and adapted geometry. To demonstrate the capabilities of AM to fabricate a variety of transient bioelectronics, several devices were printed and presented in Figure 1b–e. This includes pressure and strain sensors as well as an electrophysiology array comporting eight electrodes.

The use of direct ink writing allows to print inks that would be challenging or impossible to process with other digital printing methods. The conductive lines are based on a composite made of shellac, which is a natural bioresorbable resin, and pentanol as a low-volatility solvent to facilitate printing. Conductivity is granted to the composite by carbon and graphite particles, reproducing a disposable conductive ink that was presented in previous work.[47] The resulting composite traces can harmlessly break apart by hydrolysis or in a standard compost. The soft matrix that supports the carbon patterns, and serves as encapsulation as well as soft dielectric in the case of the pressure sensor, is POMaC polymer. Despite the comparatively more established nature of PGS as a 3D printable bioresorbable elastomer, we direct our attention toward POMaC due to several compelling factors. POMaC offers a broader spectrum of mechanical properties compared to photocurable variants of PGS, which have Young's moduli of typically a few hundreds of kPa. Further thermal curing of PGS requires temperatures above 120 °C,[51] which may pose compatibility challenges with transient inks and their binders. POMaC demonstrates excellent compatibility with the fabrication of soft electronics, typically exhibiting a Young's modulus in the range of 0.5–1.5 MPa, which is comparable to commonly used polydimethylsiloxane (PDMS) elastomers in flexible and stretchable electronics.[52] Moreover, POMaC offers several advantageous properties that make it a suitable substrate for functional devices. It exhibits remarkable thermal stability for a degradable elastomer, withstanding temperatures exceeding 200 °C.[53] Furthermore, its degradation kinetics are reasonably slow, occurring over the course of months.[54] These characteristics have captured the attention of previous investigations, positioning POMaC as a promising substrate and packaging
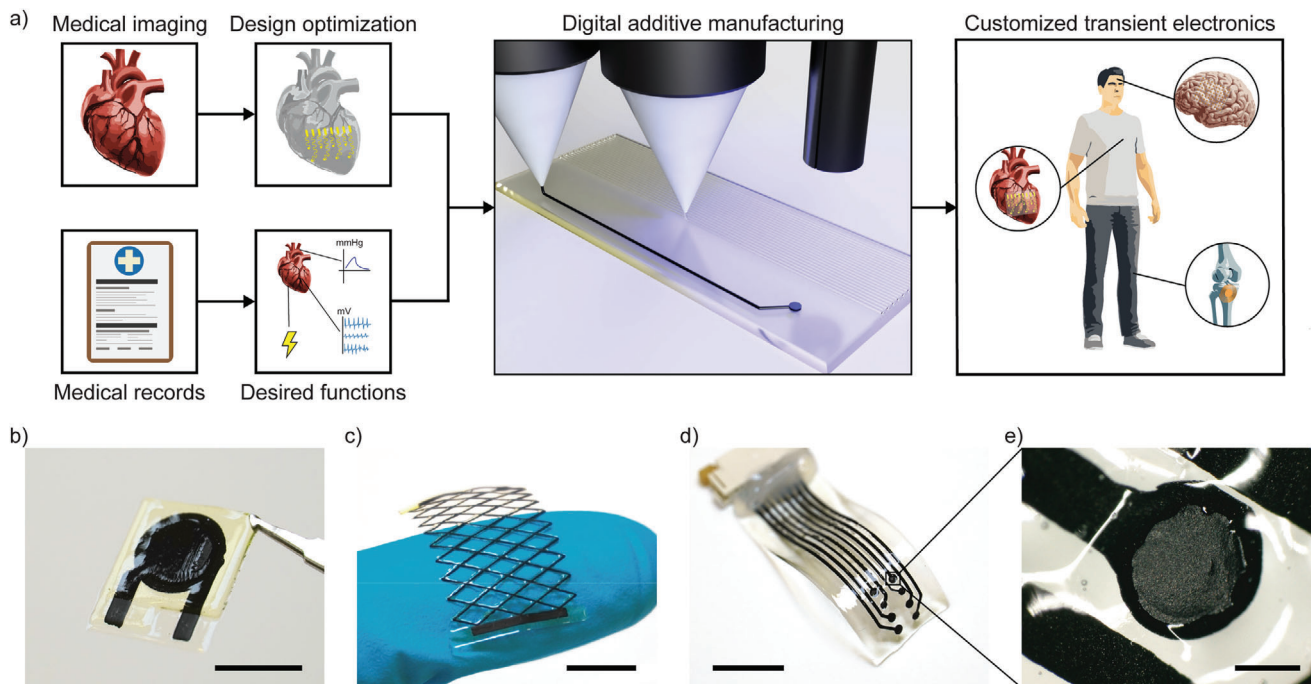
Figure 1. Additive manufacturing of customizable transient electronics. a) Illustration of the concept of using digital additive manufacturing to enable transient implantable electronics with customized forms and functions. b) DIW printed pressure parallel plate capacitor as pressure sensor (scale bar: 10 mm). c) DIW printed stretchable mesh as strain sensor. (scale bar: 10 mm). d) DIW printed electrode array (scale bar: 10 mm). e) Close-up view of an electrode (scale bar: 500 µm).

material for various implantable bioelectronic applications, or for recyclable and green electronics.[11,53] These properties facilitate the integration of conductive inks on the POMaC layer and subsequent encapsulation and curing. First, we seek to optimize the direct ink writing of POMaC polymer.

2.2. Synthesis and Printing of POMaC Pre-Polymer

POMaC is obtained through a solvent-free polycondensation reaction of benign monomers (citric acid, 1,8-octanediol and maleic anhydride), which results in a pre-polymer in the form of a viscous gel. POMaC pre-polymer is readily UV-curable owing to the vinyl group in its backbone, thereby avoiding the use of toxic reagents in the synthesis, such as those required for acrylation. In our case, photo-crosslinking is enabled by the addition of 5 wt% Irgacure 2959, a common photo-initiator used in previous investigations on POMaC.[11,35] Further cross-linking can be achieved by thermal curing at 80 °C, causing esterification of the carboxylic acid and hydroxyl groups remaining from the citric acid. The dynamic viscosity of the pre-POMaC as a function of the shear rate is shown in **Figure 2a** and the gel displays a Newtonian behavior with a viscosity of 165 Pa s. This viscosity is compatible with direct ink writing[26] and may prevent excessive ink flow during UV photopolymerization. As POMaC does not display a shear-thinning behavior, photopolymerization is key to maintaining its shape after printing. The change in the rheology of POMaC under UV illumination is shown in Figure S1 (Supporting Information), and crossover is observed after roughly one minute of exposure at 10 mW cm⁻². Ideal materials for direct ink writing

present shear-thinning behavior, allowing easier dispense under pressure and shape fidelity after deposition.[16] Therefore, a thorough investigation of the printability of POMaC pre-polymer was conducted. The printing behavior of the POMaC pre-polymer was systematically studied as a function of selected printing parameters, namely the dispense gap, printing speed, and inlet pressure, as depicted in Figure 2b. The parameters were varied respectively between 40 and 100 µm for the dispense gap, 10 and 50 mm⁻¹ s for the printing speed, and 30 and 80 psi (≈207 to 552 kPa). The objective of this analysis was to optimize the resolution and uniformity of the prints, enabling precise 3D deposition of POMaC.

These experiments were conducted with a ceramic nozzle with an internal diameter of 125 µm. For each parameter combination, lines were printed over a 15 mm distance and subsequently cured using the UV LED of the printer. For the photopolymerization, the LED was used at full power, at a working distance of 25 mm (corresponding to an irradiance of 3 W cm⁻² over 3 mm diameter area) and with a speed of 0.5 mm s⁻¹ to ensure full curing. The resulting lines were scanned using a confocal laser microscope. This process was repeated four times for each parameter combination, with a scan example shown in Figure 2b. The 3D scan of each printed line allowed us to extract several parameters, including the average line height, average line width, height variability, and width variability. The variabilities were calculated by dividing the standard deviation of the respective metric (height or width) by the average value of that metric across the entire print. The extracted values are displayed in Figure 2c,d. As expected,[55] the line width and height monotonically decrease with increasing printer speed, as seen in Figure 2c, here for a fixed pressure of 60 psi (≈414 kPa). However, when considering the height and
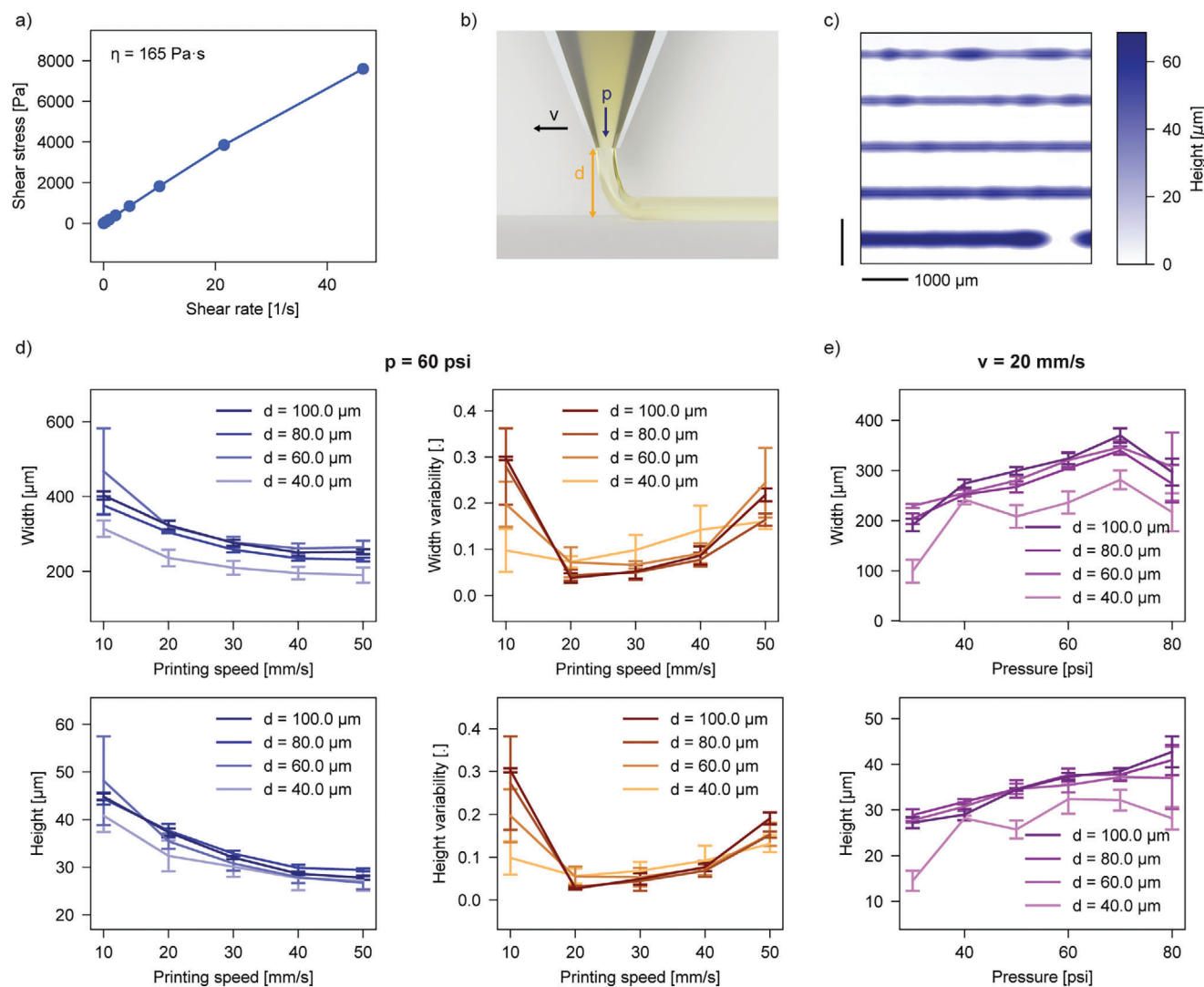
**ADVANCED
SCIENCE NEWS**

www.advancedsciencenews.com

**ADVANCED
ELECTRONIC
MATERIALS**

www.advelectronicmat.de

Figure 2. Optimization of POMaC printing by direct ink writing. a) Shear stress-shear rate behavior of POMaC pre-polymer. b) Printing parameters that are studied for the optimization of the deposition behavior (d: dispense gap, p: inlet pressure, v: printing speed). c) Example of optically scanned printed lines, with printing speeds from 10 to 50 mm s^{-1} (from bottom to top), for a pressure of 60 psi and a dispense gap of 60 µm. d) Influence of printing speed and dispense gap on the width (top left), width variability (top right), height (bottom left) and height variability (bottom right) of the printed lines for a pressure of 60 psi. e) Influence of the pressure and dispense gap on the width (top) and height (bottom) of the printed lines for a printing speed of 20 mm s^{-1}.

width variabilities, it is observed that a minimum value of ≈5% is reached at a printing speed of 20 mm^{-1} s, indicating the most consistent line quality. The dispense gap, on the other hand, appears to have negligible influence on the printing behavior for values above 40 µm, which is advantageous. This eliminates the need for precise control of the dispense gap with an accuracy of <10 µm, which can be challenging. Therefore, a printing speed of 20 mm^{-1} s was selected to maximize line homogeneity and minimize printing defects.

Figure 2d shows the width and height of printed lines as a function of the pressure and the dispense gap. Regarding the effect of pressure, both the height and width of the printed lines increase linearly with higher inlet pressure, except at 80 psi where instability is observed, due to leakage occurring in the nozzle system. To strike a balance between resolution and layer thick-

nesses, a pressure of 60 psi was chosen for further prints. For this experiment as well, the dispense gap has minimal influence above 40 µm. The minimal feature width that can be achieved reliably with these parameters is ≈250 µm, which corresponds to a spreading ratio (line width divided by nozzle diameter) of 2. This could be further improved by adding rheology modifiers to the POMaC ink to obtain a more pronounced shear-thinning behavior, preventing the spreading of the pre-polymer gel after printing.[56] However, the use of such modifiers should be approached cautiously, as their degradability would need to be assessed. Moreover, they could potentially affect the mechanical properties and curing dynamics of the POMaC, and could lead to nozzle clogging. In the current approach, the structural stability of the polymer after deposition relies mainly on its high viscosity and immediate application of UV photopolymerization. This

methodology has been successfully employed with fast-curing PGS acrylate, achieving spreading ratios on the order of 1.7.[33] Notably, delaying the UV curing of the lines by 30 minutes resulted in significantly degraded resolution and increased spreading ratio, as depicted in Figure S2 (Supporting Information). To enhance print resolution, one possible strategy could be to increase the ratio of maleic anhydride during synthesis, as this would increase the presence of vinyl bonds,[54] which would potentially result in an increased rate of cross-linking. Another approach is to perform the deposition under constant UV illumination, as demonstrated in previous studies.[33,34] However, it should be noted that this would require a considerable reduction in printing speed due to the slower photopolymerization kinetics of POMaC polymers. Figure S3 (Supporting Information) shows a summary of the printability of POMaC pre-polymer as a function of dispense pressure and printing speed, where the different dispense regimes that were observed are illustrated and a quantitative assessment of print quality is provided. In general, high pressures and slow speeds tended to cause an accumulation of ink leading to unequal lines, while low pressures and high printing speeds would lead to incomplete lines being printed due to insufficient material being deposited. Based on this optimization process, a printing speed of 20 mm s^{-1} and a pressure 60 psi were deemed optimal for the uniform dispense of POMaC pre-polymer.

With the aforementioned set of chosen parameters (printer speed: 20 mm s^{-1}, pressure 60 psi and a dispense gap of 80 µm), 2D single layers of POMaC polymer were printed and the influence of the interline distance on the layer thickness was examined (**Figure 3a**). Squares of 10 × 10 mm were printed with line spacings of 300, 200, 150, and 100 µm, respectively. The thicknesses obtained for these line spacings range from a minimum of 30 µm to a maximum of 120 µm. The optical profilometry scans of the squares are shown in Figure 3a, averaged over three samples. The squares printed with 300 µm line spacing show some raster effects and average ≈30 µm in thickness, and line spacing above this value were not investigated due to considerable raster. As expected, larger thicknesses can be obtained by decreasing the line spacing, up to over 100 µm for a line spacing of 100 µm. The pre-polymer remains a gel before photopolymerization, and the printed lines favorably flow together during printing, leading to smooth surfaces. This also leads to the presence of shoulders at the edge of the square of ≈20 µm in thickness in the printed squares which are more marked when using a line spacing of 100 µm. A line spacing of 200 µm is chosen for further experiments, as it leads to the more uniform prints. This line spacing results in layers of ≈50 µm thickness.

In order to validate the optimized parameters for the 3D direct-ink-writing of POMaC pre-polymer, up to 10 layers of 10 × 10 mm were stacked, with every layer being cured by UV before printing the next one. As evidenced in Figure 3b, the layers can be stacked reliably without collapsing or a rough surface preventing further printing (examples of printed stacks can be found in Figure S4, Supporting Information). The thickness of the print scales linearly with the number of printed layers, each layer averaging 50.3 µm. This printing method can be used to create patterned surfaces, as shown for instance in Figure 3c, where a grid with lines and holes of 250 µm is printed in 10 layers. Topologies in the third dimensions can also be attained repeatably with
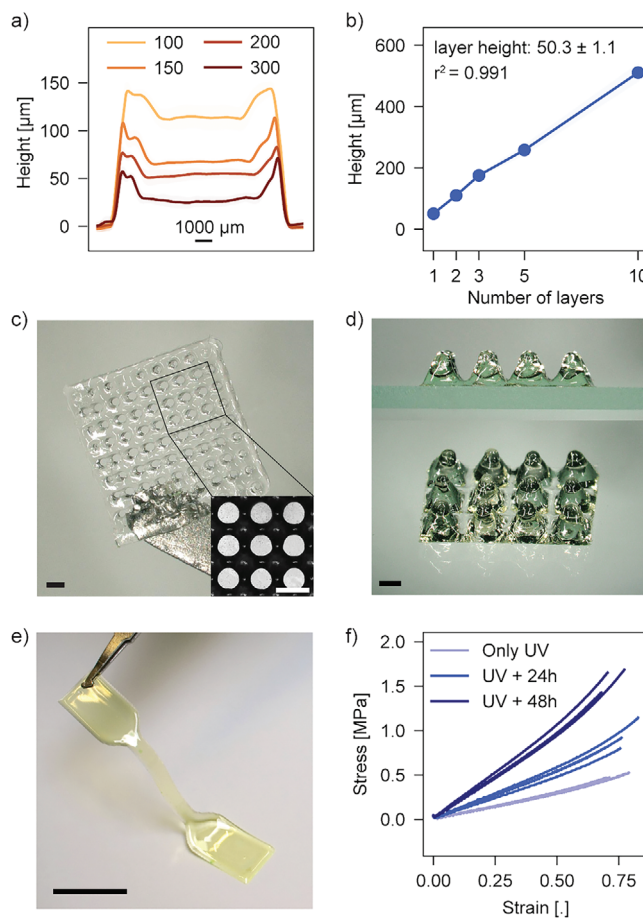

Figure 3. 3D direct ink writing of POMaC polymer. a) Effect of the line spacing on the layer height and shape. b) Height of the print versus the number of layers printed. c) Patterned POMaC surface consisting of 10 printed layers, with a zoomed in view of the features in the inset (scale bars: 500 µm). d) Example of 3D printed pyramid array (scale bars: 1 mm). e) 3D printed POMaC dogbone for mechanical properties characterization (scale bar: 10 mm). f) Stress-strain curves for POMaC with different esterification times after printing and UV curing.

3D-printed POMaC. Square-base pyramids arrays (each pyramid with a height of 2 mm and a base of 2 × 2 mm side, 42 layers total) were printed as an illustration of the capability of producing 3D structures and topologies (Figure 3d). Satisfying shape fidelity is achieved for the 3D fabrication of macroscale structures with features of a few hundred micrometers in size. A confocal microscope scan of the surface of the pyramids is shown in Figure S5 (Supporting Information), compared to the original design file.

Finally, the mechanical properties of POMaC can be tuned in terms of Young's modulus according to the curing conditions. To demonstrate this, dogbones (see Figure 3e) were printed with a thickness of 250 µm by stacking 5 layers, and their stress-strain curves to failure were measured (Figure 3f). The Young's modulus increases from 0.59 ± 0.01 MPa for the POMaC that underwent only photopolymerization to 1.90 ± 0.09 MPa after 48 h of curing at 80 °C. The mechanical properties for the different curing conditions are reported in Figure S6 (Supporting Information). The results obtained here indicate stiffer mechanical
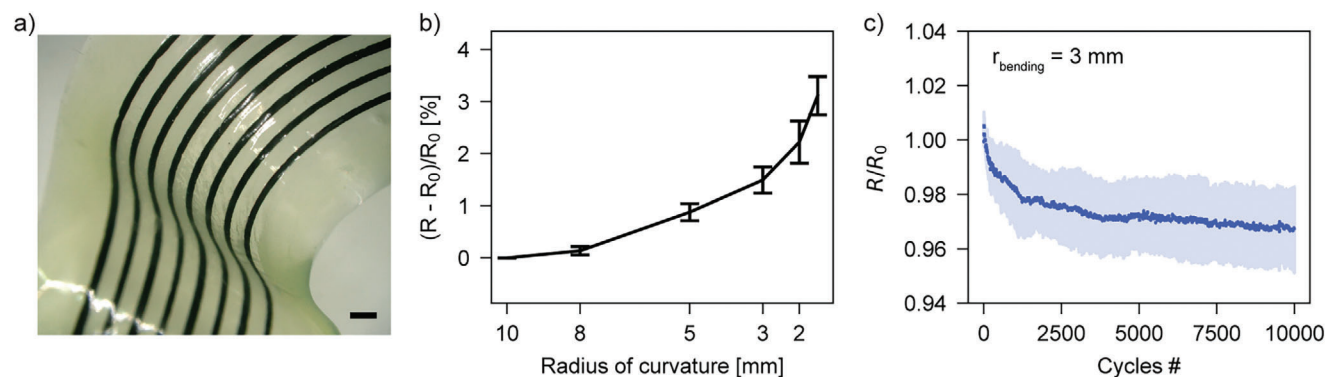
**ADVANCED
SCIENCE NEWS**

www.advancedsciencenews.com

**ADVANCED
ELECTRONIC
MATERIALS**

www.advelectronicmat.de

Figure 4. Integration of carbon conductors with POMaC. a) Optical image of fully printed carbon conductors encapsulated in POMaC (scale bar: 1 mm). b) Relative change of resistance of the carbon tracks on POMaC as a function of the bending radius (n = 6). c) Relative change of resistance during cyclic bending of carbon lines on POMaC (with a bending radius of 3 mm at 1 Hz, n = 6).

properties than as in the original publication on the synthesis of POMaC,[54] which is likely due to the higher concentration of photo-initiator and longer UV curing time, resulting in more crosslinking. For further experiments, a 48-hour esterification of POMaC at 80 °C was conducted following printing and UV curing of the layers.

Achieving conformability to the intricate geometries of organs such as the brain, gut, or heart is crucial for personalized implantable electronics, as it ensures optimal sensing capabilities. The critical radius required for a film to spontaneously wrap around a rounded shape can be estimated[17] in our case to be between 3.6 and 6.2 mm for a 200 μm POMaC film.

2.3. Integration of Conductive Carbon-Based Ink

We used a composite ink made of non-toxic and renewable materials (carbon, graphite, and shellac), as presented in a recent publication.[47] It has a conductivity of ≈1000 S m^{-1}, to embed electrical functionalities in the POMaC structures. The water-barrier properties of shellac, particularly notable for a bioresorbable material, along with the incorporation of non-oxidizing carbon and graphite components, contribute to the preservation of its conductive properties in aqueous environments. The dispense of the conductive layer and its morphology and integration with the POMaC structure is key for the performance of these transient electronic devices. Therefore, the printing behavior of the carbon ink on POMaC by DIW was systematically investigated, considering the aforementioned dispense parameters and for a fixed pressure of 10 psi, and the results are presented in Figure S7 (Supporting Information). Similarly to POMaC, the height of width of printed lines were found to decrease with increasing printing speeds, while the variability in the printed lines increased sharply for printing speeds above 30 mm s^{-1}. A smaller dispense gap led to thinner lines, but a higher variability when the smallest value was used (40 μm). As a result of this optimization, lines with an average width of ≈300 μm and average height of 30–35 μm are achieved with a printing speed of 30 mm s^{-1} and a dispense gap of 60 μm, with satisfying height and width variabilities below 5%. Fully encapsulated carbon lines are shown in **Figure** 4a and a scanning electron microscope (SEM) image

profile section of the 3D printed POMaC and carbon composite is shown in Figure S8 (Supporting Information). Notably, this shows that the conductor can be fully encapsulated in POMaC without noticeable diffusion at the interface.

As a next step, the mechanical stability of the printed and encapsulated carbon lines when statically and dynamically bent was evaluated. Bending down to a radius of 1.5 mm leads to an average relative increase of resistance of 3.1% (Figure 4b). A cyclic bending experiment was also performed at a bending radius of 3 mm, and the resistance over 10 000 cycles decreases by 3%, as shown in Figure 4c. A similar decrease in resistance has been observed in previous research on carbon black composites,[57] and could have a deleterious effect on the performance stability of resistance-based sensors. We note, however, that most of the decrease in resistance happens in the first 1000 cycles, with less than 1% change over the last 9000 cycles. This suggests that stable performance could be attained after sensor pre-cycling, which has been proposed in the past for compliant piezoresistive sensors.[19,58]

2.4. Fabrication and Characterization of 3D Printed Transient Devices

To demonstrate the capabilities offered by this process, we fabricated 3D-printed transient sensors. Biomechanical measurements, such as in vivo pressure and strain measurements, are of interest for post-surgical monitoring. Devices to measure such parameters have been proposed for transient applications targeting intracranial pressure monitoring,[9,59,60] blood vessel deformations,[61] cardiovascular postoperative care,[62] or tendon healing.[11] By subsequent printing of POMaC and carbon circular electrodes layers, as illustrated in **Figure** 5a, a parallel plate capacitor with a soft sensing interlayer was fabricated. The device was assessed for pressures ranging up to 1500 kPa, corresponding to values found notably in a normal human knee during movement.[63] Figure 5b shows an example dynamic response in terms of normalized capacitance change to the applied pressure, where it can be seen that the capacitance change tracks the applied pressure. The response curve of the capacitor is reported in Figure 5c, for 10 loading and unloading cycles. The
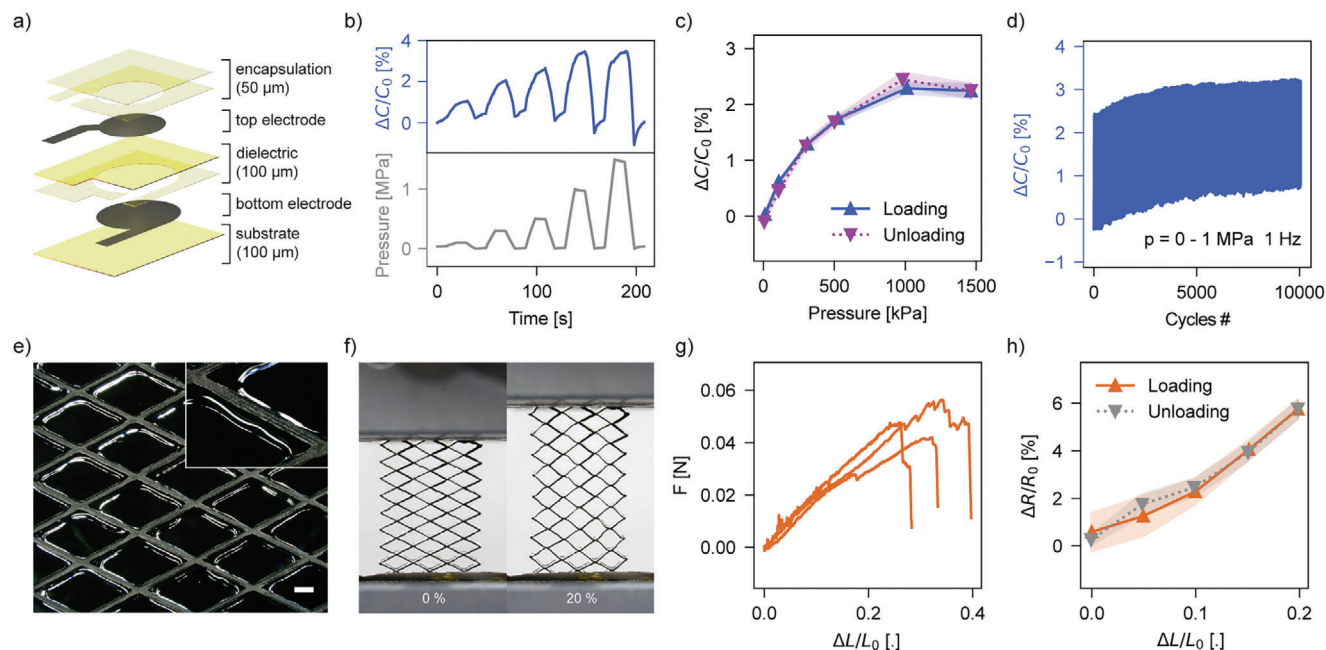
Figure 5. Mechanical sensors printed by DIW. a) Exploded view of the layers printed for the fabrication of a parallel plate capacitive pressure sensor. b) Relative response of the capacitive sensor (blue) to increasing applied pressures (grey). c) Response of the capacitive sensor to applied pressures for increasing (blue) and decreasing (purple) loads (n = 10 cycles). d) Response of the capacitive sensor to a cyclic load of 1 MPa at 1 Hz. e) Optical microscope image of the DIW printed stretchable conductive mesh pattern made of carbon on POMaC (inset: close-up view, scale bar: 1 mm). f) The printed conductive mesh pattern at rest and under a 20% axial deformation. g) Force-relative deformation curves for the mesh pattern (n = 3 devices). h) Response in terms of relative resistance change to deformation for a proof-of-concept strain sensor for increasing (orange) and decreasing (grey) relative axial deformations (n = 10 cycles).

response can be approximated as linear until 1000 kPa, and a sensitivity of 0.0029% kPa^{-1} ($r^2 = 0.93$) can be extracted. Above this pressure, the response reaches a plateau, which might be due to the relatively thick carbon electrodes clamping the POMaC polymer and limiting deformation. As expected, the sensor sensitivity could be improved by taking approaches to structure or introduce mesoscale porosity in the POMaC dielectric.[64] The design shown here, however, allows for a pressure sensing range that is on the higher end, even for pressure sensors fabricated with conventional methods and materials.[64] Based on the pressure range attained and after further application-specific characterization, this type of transient sensors could be implemented as soft wearables for diagnosis or as e-skin for eco-friendly robotics.[64,65] To further validate the stability of the pressure sensor, it was subjected to a pressure of 1000 kPa (corresponding to 100 N) for 10 000 cycles at 1 Hz, and the result of that experiment is shown in Figure 5d. The unloaded capacitance increases over to first 5000 cycles by 0.54% and stabilizes, with only 0.18% variation over the last 5000 cycles (drifting at a rate of <0.04% per 1000 cycles). This increase in capacitance is likely due to relaxation effects occurring in the viscoelastic POMaC film.

Stretchability is of interest for implanted electronics, with the soft tissues of the body undergoing deformations of 10–20% for the heart and tendons, for example.[66] The conductive carbon composite we use in this work is not inherently stretchable, yet the versatility of our additive manufacturing platform permits to engineer stretchability in devices. To this end, we printed a POMaC substrate layer (thickness 100 μm) and a conductive carbon layer patterned in a diamond mesh pattern, as shown in

Figure 5e, as stretchable structure. The resulting devices are displayed (unconstrained and under 20% relative axial deformation) in Figure 5f. The meshes undergo mechanical failure at an average 34% elongation. Failure is likely due to cracking of the carbon layer and mechanical mismatch with the soft elastomeric substrate (Figure 5g), which lead to local concentration of stresses. As proof of concept, the meshes were used as strain sensors, and their response in terms of resistance change for up to 20% axial deformation, at a strain rate of 1%/s, is shown in Figure 5h. Some hysteresis was observed in the stretchable interconnects, and the degree of hysteresis (as the maximal difference between the loading and unloading curves divided by the full-scale output) was calculated to be 6.4%. The printed strain sensor displays a gauge factor of 0.25 ($r^2 = 0.88$). The gauge factor is low, which is consistent with the use of a structure that serves to limit the strain in the carbon layer and allow to increase the sensing range.

Neuromuscular interfaces allow communication between biological tissues and electronic devices, and perform key monitoring or stimulation functions in clinical applications. Bioresorbable electrodes have been proposed for applications such as electrocorticography[12,59] or nerve stimulation.[67] We fabricated an electrode array consisting of 8 electrodes of diameter 500 μm, with the array having a surface area of 34 × 13 mm^2. The electrode array is shown in **Figure 6a** as well as a SEM image of one electrode, where it can be seen that the carbon composite creates a rough surface with a high effective area. Electrode impedance is a key metric to determine the signal quality and signal-to-noise ratio in ECoG recordings.[68] The impedance spectra of the printed ECoG array in phosphate-buffered solution are shown in
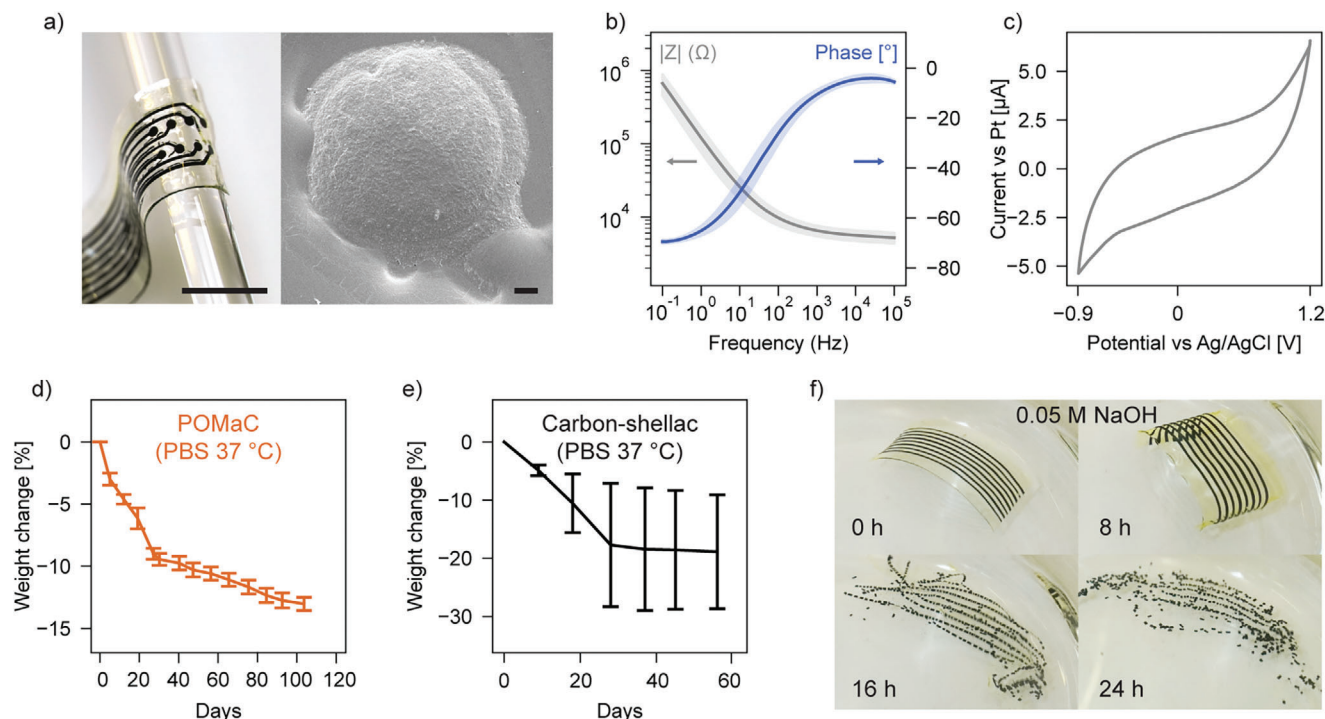
**ADVANCED
SCIENCE NEWS**

www.advancedsciencenews.com

**ADVANCED
ELECTRONIC
MATERIALS**
Open Access

www.advelectronicmat.de

Figure 6. Transient printed electrode array and materials degradation study. a) Image of the electrode array around a 3 mm radius glass rod (scale bar: 10 mm), SEM image of one electrode (scale bar: 100 µm). b) Magnitude of the electrode impedance versus frequency in PBS (n = 8). c) Cyclic voltammogram for a carbon electrode, at a scan rate of 50 mV s^{-1}. d) Relative weight change of POMaC samples immersed in PBS at 37 °C (n = 7). e) Relative weight change of carbon-shellac samples immersed in PBS at 37 °C (n = 5). f) Accelerated degradation of carbon-shellac lines embedded in POMaC in 0.05 NaOH.

Figure 6b. The impedance at 1 kHz is on average 6.5 ± 1.0 kΩ, and the cutoff frequency is 79 ± 36 Hz (n = 8). These characteristics are similar to those from electrodes of the same size found in the literature[69] and therefore suggests that they could be applicable for the recording of biopotentials. Carbon electrodes are also favorable for delivering electrical stimulation, in particular due to their wider electrochemical window compared to Pt electrodes, for instance.[70] A linear sweep voltammetry (LSV) was conducted to confirm this and is shown in Figure S9 (Supporting Information), where it can be seen that no water electrolysis occurs between −0.9 and 1.2 V. Cyclic voltammetry (CV) for a representative electrode and conducted within the water window is shown in Figure 6c. The charge storage capacity calculated from the CV measurements is 21.74 ± 6.15 mC cm^{-2} (n = 4), which is reasonably high and suggests that these electrodes could be appropriate for electrical stimulation applications.[71]

Finally, the materials constituting the devices presented above were studied in terms of their degradation in PBS at 37 °C. Figure 6d shows the mass loss percentage for circular POMaC specimen of diameter 18 mm and thickness 267 ± 8 µm as a function of the days of incubation in PBS. POMaC, after photocrosslinking and 48 h heat curing at 80 °C, degrades at an average rate of ≈0.89% per week, in line with the original publication describing the synthesis of this polymer.[53,54] The degradation happens at a faster rate in the first three weeks (which may correspond to smaller chains being degraded) and reaches a steadier rate from the third week. Similarly, square carbon-shellac samples of size 10 × 10 mm^2 and average thickness 33.13 ± 8.18 µm

were prepared and incubated in PBS at 37 °C (Figure 6e). An average mass loss rate of 2.6% per week was observed. However, this corresponds to both surface erosion as well as breaking off of small pieces of conductive composite, which explains the high variability in the data. The disintegration of carbon lines in a POMaC structure array was also characterized under conditions of accelerated hydrolysis in 0.05 NaOH (pH 12.7). Images of the breakdown of the device are shown in Figure 6f and the POMaC encapsulation dissolves in ≈16 h, leaving non-hydrolysable carbon particulates.

3. Conclusion

In summary, we have demonstrated, for the first time, a platform for the monolithic fabrication by digital 3D additive manufacturing of soft sensors and bioelectronics from degradable materials. The easily customizable devices are enabled by the 3D printing of the degradable elastomer POMaC as well as carbon conductive layers, whose printing behavior are thoroughly investigated. The influence of the dispense parameters, e.g. pressure, dispense gap, and printer speed, on the morphology of printed layers is studied and optimal parameters are determined in order to repeatably print features of 200–300 µm in width and layers of thicknesses between 30 and 50 µm. The printing behavior can be modulated by adapting these parameters, and could be further modified with a different nozzle size, if smaller features or thicker layers are targeted. The process is shown to be compatible with the fabrication of 3D shapes of several millimeters with

**ADVANCED
SCIENCE NEWS**

www.advancedsciencenews.com

**ADVANCED
ELECTRONIC
MATERIALS**

www.advelectronicmat.de

no collapse of the layers. In order to improve the shape fidelity of the printed POMaC, more studies are needed on degradable rheology modifiers and fillers.

An ink based on carbon particles and bioresorbable resin shellac is printed on the degradable elastomer as a conductive layer. The printed carbon embedded in POMaC is also demonstrated to be conformable and can be bent down to 2 millimeters while maintaining its electrical conductivity, and cyclic bending for 10 000 cycles leads to only a small variation in resistance. This platform for transient customized electronics allows the demonstration of functional devices for the acquisition of relevant signals. A multilayer pressure sensor based on a parallel plate capacitor design allows for the monitoring of uniaxial pressures up to 1500 kPa and up to 10 000 cycles at a frequency of 1 Hz, which could be suitable for the recording of human joint pressure during movement. Stretchable conductive patterns are also demonstrated, and used in proof-of-concept experiments as strain sensors up to 20% relative deformation. An 8-electrode array for electrocorticography, electrocardiograph, or electromyography is demonstrated. The impedance of the printed electrodes is 6.5 ± 1.0 kΩ at 1 kHz with a cutoff frequency of 79 ± 36 Hz, which is in line with values obtained for microfabricated non-degradable electrode arrays. Finally, the materials used in this 3D manufacturing platform are shown to degrade in physiological conditions on a timescale of months.

Here, we demonstrated proof-of-concept prototypes and further research remains to validate these sensors for a specific application. In particular, in order to utilize the transient electronic devices presented in this work as ecoresorbable wearables or bioresorbable implants, further work is required on the functionality and degradation of the sensors in the relevant environment. Notably, the effects of the degradation of the carbon traces should be further studied to ensure its harmless degradation in the desired setting. The ink also contains pentanol, which is not biocompatible, but we expect it to fully evaporate from the traces during the POMaC thermal curing and/or a subsequent DI water wash.

Finally, future work could leverage the facile customization enabled by direct ink writing, in combination with mathematical optimization methods such as generative design or topology optimization. Additive manufacturing makes it possible to easily translate in silico designs into functional devices, which allows to quickly iterate and optimize prototypes for a specific application. With this approach, transient wearables and implants for temporary applications could be generated from medical imaging and optimized in terms of layout, mechanical properties, and topology to attain higher recording quality and better conformability.

4. Experimental Section

POMaC Pre-Polymer Synthesis and Characterization: POMaC was synthesized similarly to previous protocols.[54] 1,8 octanediol, citric acid, and maleic anhydride (Sigma-Aldrich) were mixed at a molar ratio of 5:2:3 in a 250 mL three-necked flask and heated to 160 °C until full melting of the reagents. The reagents were then polymerized at 140 °C for 3 h under nitrogen flux, with a needle in the third neck to allow for the evacuation of the water resulting from the polycondensation reaction. After cooling to room temperature, the pre-polymer was dissolved in THF and

purified by drop-wise purification in DI water for 2 h, decanted, and dried for a week under vacuum. The pre-polymer was then mixed with 5 wt% photonitiator 2-hydroxy-4′-(2-hydroxyethoxy)–2-methylpropiophenone (Ir-gacure 2959). The rheology of POMaC was characterized with a DHR-2 Rotational Rheometer (TA Instruments), using a cone and plate geometry (1000 µm). The dynamic oscillatory time sweep was conducted under 10 mW cm^{-2} UV exposure at 365 nm, at 1 Hz, and under 0.5% strain.

POMaC Printing Optimization: A nScrypt 3Dn-300 printer was used for all the 3D printing experiments conducted in this work. A Smart-PumpTM100 attachment was used for the controlled dispense of POMaC pre-polymer, with a zirconia-toughened alumina nozzle (outer diameter: 175 µm, inner diameter: 125 µm). The valve rod position settings for open and closed positions were set to 1.9 and 1.4 mm respectively. For the line dispense optimization, lines of 15 mm were printed on polyimide films and subsequently UV-cured at a speed of 0.5 mm s^{-1}. For the layer printing optimization, 10 × 10 mm squares were printed and subsequently UV cured with a speed of 2 mm s^{-1}, with the same line spacing as for the printing. UV curing was carried out with the printer UV head at full power and at a distance of 25 mm (365 nm, peak irradiance: 8,000 mW cm^{-2}). Printed shapes were covered in a thin layer of sputtered gold (5–10 nm) to ensure opacity and precise surface scanning. The shapes topologies were measured using a laser scanning confocal microscope (Keyence VK-X1000). The height data was corrected for surface shape, the printed lines were automatically detected and the metrics mentioned before were calculated as described. This analysis was carried out in a custom python script. Slicing and generation of printing instructions (in.gcode format) was carried out in Prusa Slicer 2.5.0 and translated project files for the 3Dn-300 printer using custom code written in python.

POMaC Pull Testing: POMaC dogbones samples were printed in 5 layers, which were each photopolymerized at a speed of 2 mm s^{-1}. The samples were printed on a polyimide substrate which was preliminarily covered with a blade-cast layer of polyacrylic acid serving as sacrificial layer. After printing, the samples were exposed to UV light (Proma 140 001, 60 W, 365 nm) for 30 min to ensure full UV curing of the polymer. The polyimide sheet with the dogbones was placed in DI water overnight and the samples were gently peeled after dissolution of the sacrificial layer and dried in air. Stress-strain curves were measured with a 340 Single Column Universal Testing System (Instron) at a strain rate of 500 mm per minute.

Carbon Ink Preparation and Printing: The carbon paste was prepared as previously described. Briefly, graphite flakes (7–10 µm, Alfa Aesar, USA), carbon black (Lion Specialty Chemicals Co., Ltd Japan) and 9.5 g of 34 wt% shellac solution in pentanol (Shellac Orange by Kremer Pigment, Germany) were mixed at a weight ratio of 4:1:9.5 at 5 min at 2350 rpm (DAC600 by Hauschild SpeedMixer, Germany). Direct ink writing of the carbon inks was conducted as for the POMaC inks, with another Smart-PumpTM100 attachment on the 3Dn-300 printer, equipped with a 125 µm internal diameter nozzle. Carbon inks were printed on blade-cast POMaC for the printing study and scanned by laser confocal microscopy as described above.

Devices Fabrication and Characterization: All the devices presented in this work were printed from the POMaC and carbon inks as described above. The carbon ink was left to dry for 20 min after subsequent printing of POMaC encapsulation, where relevant. Direct ink writing was performed standard 4-inch single-side polished silicon wafer which was preliminarily covered with a sacrificial layer of spin-coated polyacrylic acid. Silicon wafers were used as carriers to ensure a flat surface during printing. The printed devices were further oven-cured at 80 °C for 48 h and released from the carriers in DI water overnight. For the bending tests, carbon interconnects encapsulated in POMaC were subjected to mechanical bending in a custom motorized setup, and the resistance values of the lines were continuously acquired with a digital multimeter (Keysight 34401A). For the pressure sensors, uniaxial pressures were applied with a single-column Universal Testing System (Instron 3340) and the capacitance values were recorded using an LCR-meter (Agilent E4980A) at 2 MHz. Electrochemical characterization of the electrode arrays was conducted on a potentiostat/galvanostat (Metrohm Autolab 8 Series, PGSTAT302N, FRA32M module) in a three-electrode configuration, with an electrode from the array serving as working electrode, a Pt wire as counter electrode and a

silver/silver chloride pellet as reference electrode. For impedance spectroscopy, a 10 mV RMS sine wave was used, for frequencies between 0.1 Hz and 100 kHz. LSV measurements were conducted between −2 and 2 V with a scan rate of 50 mV s^{-1}, and CV measurements were performed between −0.9 and 1.2 V with a scan rate of 50 mV s^{-1}.

Degradation Experiments: POMaC samples of 18 mm diameter and thicknesses of 267 ± 8 µm were prepared and incubated in PBS at 37 °C in individual 12 mL glass vials. The samples were weighed with a precision scale (Metler Toledo XSR105) after light rinsing in DI water and drying for 2 h under vacuum at 50 °C. Carbon ink square samples with a side dimension of 10 mm and an average thickness of 33.13 ± 8.18 µm were incubated and weighed as described above for the POMaC samples. The accelerated aging test was conducted in 0.05 M NaOH solution at room temperature.

Supporting Information

Supporting Information is available from the Wiley Online Library or from the author.

Conflict of Interest

The authors declare no conflict of interest.

Data Availability Statement

The data that support the findings of this study are available from the corresponding author upon reasonable request.

[1] S.-W. Hwang, H. Tao, D.-H. Kim, H. Cheng, J.-K. Song, E. Rill, M. A. Brenckle, B. Panilaitis, S. M. Won, Y.-S. Kim, Y. M. Song, K. J. Yu, A. Ameen, R. Li, Y. Su, M. Yang, D. L. Kaplan, M. R. Zakin, M. J. Slepian, Y. Huang, F. G. Omenetto, J. A. Rogers, *Science* **2012**, *337*, 1640.

[2] W. B. Han, J. H. Lee, J. Shin, S. Hwang, *Adv. Mater.* **2020**, *32*, 2002211.

[3] K. K. Fu, Z. Wang, J. Dai, M. Carter, L. Hu, *Chem. Mater.* **2016**, *28*, 3527.

[4] G. D. Cha, D. Kang, J. Lee, D. Kim, *Adv. Healthcare Mater.* **2019**, *8*, 1801660.

[5] C. Li, C. Guo, V. Fitzpatrick, A. Ibrahim, M. J. Zwierstra, P. Hanna, A. Lechtig, A. Nazarian, S. J. Lin, D. L. Kaplan, *Nat. Rev. Mater.* **2020**, *5*, 61.

[6] C. Dagdeviren, S.-W. Hwang, Y. Su, S. Kim, H. Cheng, O. Gur, R. Haney, F. G. Omenetto, Y. Huang, J. A. Rogers, *Small* **2013**, *9*, 3398.

[7] M. A. Meitl, Z.-T. Zhu, V. Kumar, K. J. Lee, X. Feng, Y. Y. Huang, I. Adesida, R. G. Nuzzo, J. A. Rogers, *Nature Mater.* **2006**, *5*, 33.

[8] A. Palmroth, T. Salpavaara, J. Lekkala, M. Kellomäki, *Adv. Mater. Technol.* **2019**, *4*, 1900428.

[9] M. Luo, A. W. Martinez, C. Song, F. Herrault, M. G. Allen, *J. Microelectromech. Syst.* **2014**, *23*, 4.

[10] S.-K. Kang, R. K. J. Murphy, S.-W. Hwang, S. M. Lee, D. V. Harburg, N. A. Krueger, J. Shin, P. Gamble, H. Cheng, S. Yu, Z. Liu, J. G. McCall, M. Stephen, H. Ying, J. Kim, G. Park, R. C. Webb, C. H. Lee, S. Chung, D. S. Wie, A. D. Gujar, B. Vemulapalli, A. H. Kim, K.-M. Lee, J. Cheng, Y. Huang, S. H. Lee, P. V. Braun, W. Z. Ray, J. A. Rogers, *Nature* **2016**, *530*, 71.

[11] C. M. Boutry, Y. Kaizawa, B. C. Schroeder, A. Chortos, A. Legrand, Z. Wang, J. Chang, P. Fox, Z. Bao, *Nat. Electron.* **2018**, *1*, 314.

[12] K. J. Yu, D. Kuzum, S.-W. Hwang, B. H. Kim, H. Juul, N. H. Kim, S. M. Won, K. Chiang, M. Trumpis, A. G. Richardson, H. Cheng, H. Fang, M. Thompson, H. Bink, D. Talos, K. J. Seo, H. N. Lee, S.-K. Kang, J.-H. Kim, J. Y. Lee, Y. Huang, F. E. Jensen, M. A. Dichter, T. H. Lucas, J. Viventi, B. Litt, J. A. Rogers, *Nat. Mater.* **2016**, *15*, 782.

[13] Y. S. Choi, R. T. Yin, A. Pfenniger, J. Koo, R. Avila, K. Benjamin Lee, S. W. Chen, G. Lee, G. Li, Y. Qiao, A. Murillo-Berlioz, A. Kiss, S. Han, S. M. Lee, C. Li, Z. Xie, Y.-Y. Chen, A. Burrell, B. Geist, H. Jeong, J. Kim, H.-J. Yoon, A. Banks, S.-K. Kang, Z. J. Zhang, C. R. Haney, A. V. Sahakian, D. Johnson, T. Efimova, Y. Huang, et al., *Nat. Biotechnol.* **2021**, *39*, 1228.

[14] X. Yu, W. Shou, B. K. Mahajan, X. Huang, H. Pan, *Adv. Mater.* **2018**, *30*, 1707624.

[15] W. Huo, J. Li, M. Ren, W. Ling, H. Xu, C. A. T. Tee, X. Huang, *Curr. Opin. Chem. Eng.* **2020**, *28*, 118.

[16] R. L. Truby, J. A. Lewis, *Nature* **2016**, *540*, 371.

[17] M. Vomero, M. F. Porto Cruz, E. Zucchini, F. Ciarpella, E. Delfino, S. Carli, C. Boehler, M. Asplund, D. Ricci, L. Fadiga, T. Stieglitz, *Biomaterials* **2020**, *255*, 120178.

[18] A. Dubey, S. Ray, *J. Neurosci.* **2019**, *39*, 4299.

[19] M. R. Binelli, R. van Dommelen, Y. Nagel, J. Kim, R. I. Haque, F. B. Coulter, G. Siqueira, A. R. Studart, D. Briand, *Sci. Rep.* **2023**, *13*, 1962.

[20] I. R. Minev, P. Musienko, A. Hirsch, Q. Barraud, N. Wenger, E. M. Moraud, J. Gandar, M. Capogrosso, T. Milekovic, L. Asboth, R. F. Torres, N. Vachicouras, Q. Liu, N. Pavlova, S. Duis, A. Larmagnac, J. Vörös, S. Micera, Z. Suo, G. Courtine, S. P. Lacour, *Science* **2015**, *347*, 159.

[21] T. Stuart, K. A. Kasper, I. C. Iwerunmor, D. T. McGuire, R. Peralta, J. Hanna, M. Johnson, M. Farley, T. LaMantia, P. Udorvich, P. Gutruf, *Sci. Adv.* **2021**, *7*, eabj3269.

[22] D. Afanasenkau, D. Kalinina, V. Lyakhovetskii, C. Tondera, O. Gorsky, S. Moosavi, N. Pavlova, N. Merkulyeva, A. V. Kalueff, I. R. Minev, P. Musienko, *Nat. Biomed. Eng.* **2020**, *4*, 1010.

[23] E. Borda, L. Ferlauto, J. Schleuniger, A. Mustaccio, F. Lütolf, A. Lücke, S. Fricke, N. Marjanović, D. Ghezzi, *Adv. Eng. Mater.* **2020**, *22*, 1901403.

[24] P. Wang, E. G. Wu, H. Uluşan, A. J. Phillips, M. R. Hays, A. Kling, E. T. Zhao, S. Madugula, R. S. Vilkhu, P. K. Vasireddy, A. Hierlemann, G. Hong, E. J. Chichilnisky, N. A. Melosh, **2023**.

[25] T. Zhou, H. Yuk, F. Hu, J. Wu, F. Tian, H. Roh, Z. Shen, G. Gu, J. Xu, B. Lu, X. Zhao, *Nat. Mater.* **2023**, *22*, 895.

[26] M. a. S. R. Saadi, A. Maguire, N. T. Pottackal, M. S. H. Thakur, M. Md. Ikram, A. J. Hart, P. M. Ajayan, M. M. Rahman, *Adv. Mater.* **2022**, *34*, 2108855.

[27] L. Nayak, S. Mohanty, S. Kumar Nayak, A. Ramadoss, *J. Mater. Chem. C* **2019**, *7*, 8771.

[28] T. J. Wallin, J. Pikul, R. F. Shepherd, *Nat. Rev. Mater.* **2018**, *3*, 84.

[29] C. L. E. Nijst, J. P. Bruggeman, J. M. Karp, L. Ferreira, A. Zumbuehl, C. J. Bettinger, R. Langer, *Biomacromolecules* **2007**, *8*, 3067.

[30] S. Pashneh-Tala, R. Owen, H. Bahmaee, S. Rekštytė, M. Malinauskas, F. Claeyssens, *Front. Phys.* **2018**, *6*, 41.

[31] C. Zhu, S. R. Kustra, C. J. Bettinger, *Acta Biomater.* **2013**, *9*, 7362.

[32] Y.-L. Wu, A. R. D'Amato, A. M. Yan, R. Q. Wang, X. Ding, Y. Wang, *ACS Appl. Bio Mater.* **2020**, *3*, 7575.

[33] Y.-C. Yeh, C. B. Highley, L. Ouyang, J. A. Burdick, *Biofabrication* **2016**, *8*, 045004.

[34] Y.-C. Yeh, L. Ouyang, C. B. Highley, J. A. Burdick, *Polym. Chem.* **2017**, *8*, 5091.

[35] D. J. Wales, M. Keshavarz, C. Howe, E. Yeatman, *ACS Appl. Polym. Mater.* **2022**, *4*, 5457.

[36] K. H. Song, C. B. Highley, A. Rouff, J. A. Burdick, *Adv. Funct. Mater.* **2018**, *28*, 1801331.

[37] A. Prasopthum, Z. Deng, I. M. Khan, Z. Yin, B. Guo, J. Yang, *Biomater. Sci.* **2020**, *8*, 4287.

[38] F. Gao, Z. Xu, Q. Liang, H. Li, L. Peng, M. Wu, X. Zhao, X. Cui, C. Ruan, W. Liu, *Adv. Sci.* **2019**, *6*, 1900867.

[39] W. Sun, A. S. Williamson, R. Sukhnandan, C. Majidi, L. Yao, A. W. Feinberg, V. A. Webster-Wood, *Adv. Funct. Mater.* **2023**, *33*, 2303659.

[40] W. Wang, Z. Li, H. Xu, L. Qiao, X. Zhang, Y. Zhao, Z. Dong, H. Huang, X. Zhao, B. Guo, *Mater. Des.* **2022**, *222*, 111041.

[41] R. Huo, G. Bao, Z. He, X. Li, Z. Ma, Z. Yang, R. Moakhar, S. Jiang, C. Chung-Tze-Cheong, A. Nottegar, C. Cao, S. Mahshid, J. Li, *Adv. Funct. Mater.* **2023**, *33*, 2213677.

[42] J. Park, S. Lee, M. Lee, H.-S. Kim, J. Y. Lee, *Small* **2023**, *19*, 2300250.

[43] Y. K. Lee, J. Kim, Y. Kim, J. W. Kwak, Y. Yoon, J. A. Rogers, *Adv. Mater.* **2017**, *29*, 1702665.

[44] S. Feng, Z. Tian, J. Wang, S. Cao, D. Kong, *Adv. Electron. Mater.* **2019**, *5*, 1800693.

[45] N. Fumeaux, D. Briand, *NPJ Flex. Electron.* **2023**, *7*, 14.

[46] C. Zhu, N. B. Schorr, Z. Qi, B. R. Wygant, D. E. Turney, G. G. Yadav, M. A. Worsley, E. B. Duoss, S. Banerjee, E. D. Spoerke, A. van Buuren, T. N. Lambert, *Small Structures* **2023**, *4*, 2200323.

[47] A. Poulin, X. Aeby, G. Siqueira, G. Nyström, *Sci. Rep.* **2021**, *11*, 23784.

[48] S. Brooks, Z. Cartwright, D. Merckle, A. C. Weems, *Polym. Compos.* **2021**, *42*, 5134.

[49] K. Kim, J. Yoo, J. Shim, Y. Ryu, S. Choi, J. Lee, H. M. Lee, J. Koo, S. Kang, *Adv. Mater. Technol.* **2022**, *7*, 2001297.

[50] K. S. Kim, W.-Y. Maeng, S. Kim, G. Lee, M. Hong, G. Kim, J. Kim, S. Kim, S. Han, J. Yoo, H. Lee, K. Lee, J. Koo, *Mater. Today Bio* **2023**, *18*, 100541.

[51] Y. Li, W. D. Cook, C. Moorhoff, W.-C. Huang, Q.-Z. Chen, *Polym. Int.* **2013**, *62*, 534.

[52] R. Moučka, M. Sedlačík, J. Osička, V. Pata, *Sci. Rep.* **2021**, *11*, 19090.

[53] B. L. Turner, J. Twiddy, M. D. Wilkins, S. Ramesh, K. M. Kilgour, E. Domingos, O. Nasrallah, S. Menegatti, M. A. Daniele, *NPJ Flex Electron* **2023**, *7*, 25.

[54] R. T. Tran, P. Thevenot, D. Gyawali, J.-C. Chiao, L. Tang, J. Yang, *Soft Matter* **2010**, *6*, 2449.

[55] L. Zhou, Q. Gao, J. Fu, Q. Chen, J. Zhu, Y. Sun, Y. He, *ACS Appl. Mater. Interfaces* **2019**, *11*, 23573.

[56] F. Ruther, J. A. Roether, A. R. Boccaccini, *Adv. Eng. Mater.* **2022**, *24*, 2101768.

[57] T. Kinkeldei, C. Zysset, N. Münzenrieder, G. Tröster, *J. Polym. Sci., Part B: Polym. Phys.* **2013**, *51*, 329.

[58] D. Yan, T. M. Bruns, Y. Wu, L. L. Zimmerman, C. Stephan, A. P. Cameron, E. Yoon, J. P. Seymour, *Adv. Healthcare Mater.* **2019**, *8*, e1900477.

[59] K. Xu, S. Li, S. Dong, S. Zhang, G. Pan, G. Wang, L. Shi, W. Guo, C. Yu, J. Luo, *Adv. Healthcare Mater.* **2019**, *8*, 1801649.

[60] D. Lu, Y. Yan, Y. Deng, Q. Yang, J. Zhao, M. Seo, W. Bai, M. R. MacEwan, Y. Huang, W. Z. Ray, J. A. Rogers, *Adv. Funct. Mater.* **2020**, *30*, 2003754.

[61] C. M. Boutry, L. Beker, Y. Kaizawa, C. Vassos, H. Tran, A. C. Hinckley, R. Pfattner, S. Niu, J. Li, J. Claverie, Z. Wang, J. Chang, P. M. Fox, Z. Bao, *Nat. Biomed. Eng.* **2019**, *3*, 47.

[62] H. Ouyang, Z. Li, M. Gu, Y. Hu, L. Xu, D. Jiang, S. Cheng, Y. Zou, Y. Deng, B. Shi, W. Hua, Y. Fan, Z. Li, Z. Wang, *Adv. Mater.* **2021**, *33*, 2102302.

[63] T. Zhou, *Healthc. Technol. Lett.* **2018**, *5*, 247.

[64] H. Wang, Z. Li, Z. Liu, J. Fu, T. Shan, X. Yang, Q. Lei, Y. Yang, D. Li, *J. Mater. Chem. C* **2022**, *10*, 1594.

[65] K.-H. Ha, H. Huh, Z. Li, N. Lu, *ACS Nano* **2022**, *16*, 3442.

[66] R. Feiner, T. Dvir, *Nat. Rev. Mater.* **2017**, *3*, 17076.

[67] J. Koo, M. R. MacEwan, S.-K. Kang, S. M. Won, M. Stephen, P. Gamble, Z. Xie, Y. Yan, Y.-Y. Chen, J. Shin, N. Birenbaum, S. Chung, S. B. Kim, J. Khalifeh, D. V. Harburg, K. Bean, M. Paskett, J. Kim, Z. S. Zohny, S. M. Lee, R. Zhang, K. Luo, B. Ji, A. Banks, H. M. Lee, Y. Huang, W. Z. Ray, J. A. Rogers, *Nat. Med.* **2018**, *24*, 1830.

[68] T. Chung, J. Q. Wang, J. Wang, B. Cao, Y. Li, S. W. Pang, *J. Neural Eng.* **2015**, *12*, 056018.

[69] C. Boehler, S. Carli, L. Fadiga, T. Stieglitz, M. Asplund, *Nat. Protoc.* **2020**, *15*, 3557.

[70] M. Vomero, E. Castagnola, F. Ciarpella, E. Maggiolini, N. Goshi, E. Zucchini, S. Carli, L. Fadiga, S. Kassegne, D. Ricci, *Sci. Rep.* **2017**, *7*, 40332.

[71] G. Schiavone, X. Kang, F. Fallegger, J. Gandar, G. Courtine, S. P. Lacour, *Neuron* **2020**, *108*, 238.